IOP PUBLISHING SCIENCE AND TECHNOLOGY OF ADVANCED MATERIALS
Sci. Technol. Adv. Mater. **9** (2008) 035013 (6pp) doi:10.1088/1468-6996/9/3/035013

A 3D tomographic EBSD analysis of a CVD diamond thin film

Tao Liu, Dierk Raabe and Stefan Zaefferer

Max-Planck-Institut für Eisenforschung, Abteilung Mikrostrukturphysik und Umformtechnik,
Max-Planck-Strasse 1, 40237 Düsseldorf, Germany

E-mail: d.raabe@mpie.de

Received 15 May 2008
Accepted for publication 23 July 2008
Published 8 October 2008
Online at stacks.iop.org/STAM/9/035013

Abstract
We have studied the nucleation and growth processes in a chemical vapor deposition (CVD) diamond film using a tomographic electron backscattering diffraction method (3D EBSD). The approach is based on the combination of a focused ion beam (FIB) unit for serial sectioning in conjunction with high-resolution EBSD. Individual diamond grains were investigated in 3-dimensions particularly with regard to the role of twinning.

Keywords: CVD diamond films, nucleation, growth, twinning, dislocation density,
3D EBSD, FIB

(Some figures in this article are in colour only in the electronic version)

1. Introduction

Because of their extreme physical properties (e.g. highest hardness, highest known value of thermal conductivity at 300 K, wide band gap (~5.5 eV), and broad optical transparency from deep ultraviolet to far infrared), polycrystalline diamond films have attracted increasing attention [1–5]. Since the properties of a diamond crystal depend on the crystallographic direction, it is important to understand the effect of film deposition parameters on the evolution of the crystallographic orientation distribution (texture) and microstructure [6–15]. For instance, in the field of mechanical properties and wear, it was observed that [100]-oriented films exhibit lower roughness and higher wear resistance than those in other crystallographic directions, which renders them suited for tribological applications [13][1]. ⟨100⟩-textured films are also ideal for heat-transport applications since the heat conductivity in the crystallographic ⟨100⟩ direction exceeds that in the ⟨111⟩ and ⟨110⟩ directions [9, 10]. It has been reported that the dark current of a (001)-oriented diamond film is much lower and more stable than that of a (111)-oriented diamond film [11]. The (111) surfaces of diamond films have a negative electron affinity, i.e. they emit electrons in the presence of a sufficiently strong electrical field; thus, (111)-oriented diamond films are the best choice for corresponding devices [16]. For optical applications, the properties of (001)-oriented diamond films are superior to those of (111)-oriented films in terms of the refractive index and extinction coefficient [11]. Beyond these basic texture-property relations [17], more specific studies on the relationship between texture and microstructure have been reported for diamond [15–31].

The above examples indicate that more detailed structure-property investigations on diamond film textures will increasingly require local characterization methods. In particular, a more comprehensive understanding of the growth dynamics of diamond films with respect to texture and grain size evolution has not yet been obtained. Although important texture results for diamond have been obtained by x-ray diffraction (XRD), electron backscatter diffraction (EBSD) provides more detailed information about the texture, grain size, and interfaces of such films [18–22, 26]. For instance, an important contribution in this area was made by Fujii *et al* [23]. In their work, the authors quantified the crystallinity, texture, and crystal size of diamond films by Raman scattering and EBSD, and they subsequently correlated the data with the propagation loss of surface acoustic waves measured at 1.8 GHz.

The potential of orientation microscopy via EBSD has recently been markedly enhanced by introducing a

---

[1] {hkl}: crystal plane; ⟨uvw⟩: crystal direction.

1468-6996/08/035013+06$30.00

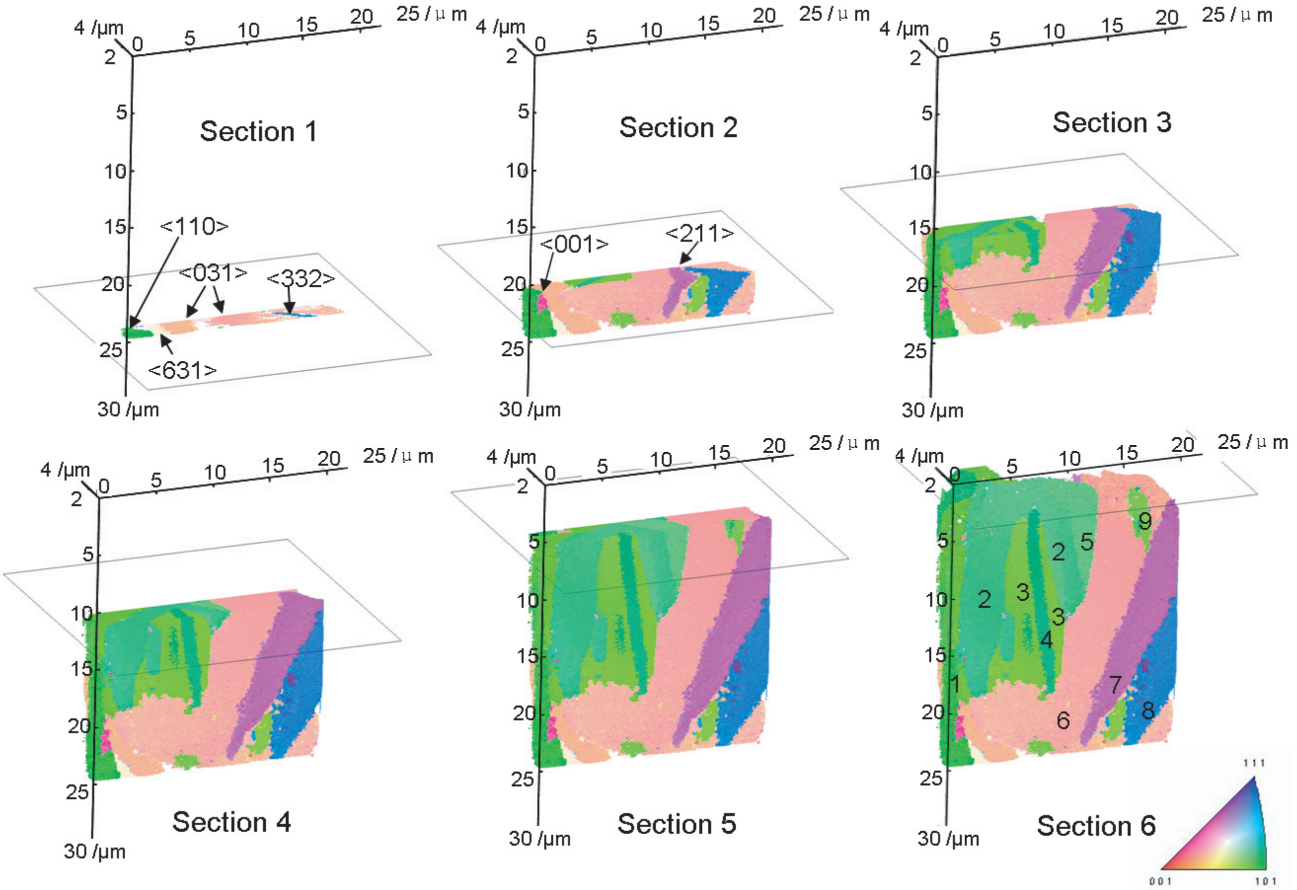

Figure 1. 3D EBSD analysis of diamond grains. 3D orientation maps at different sections on 6 different planes perpendicular to the growth direction. Section 1 is close to the nucleation zone and section 6 is the final growth front. Orientation maps are color coded according to the crystallographic direction parallel to the growth direction.

joint high-resolution, field-emission SEM–EBSD setup in conjunction with a focused ion beam (FIB) system in the form of a 3D crystal orientation microscope (3D EBSD) [25].

Therefore, in this study we present for the first time an experimental characterization of the microstructure and microtexture at the initial nucleation stage in a non-freestanding diamond thin film using 3D EBSD.

2. Experimental

2.1. Diamond film synthesis

A non-freestanding CVD diamond film was prepared by the high-power, direct-current arc plasma jet method, operated in gas recycling mode [32–34]. The substrate was a molybdenum sample of 65 mm diameter and 10 mm thickness. The substrate was kept at 1000 °C during deposition (±20 °C). The methane concentration in the hydrogen feeding flow was 1%. Since the microscopic roughness of the substrate promotes nucleation [35, 36], the substrate was polished using diamond powder and cleaned in an ultrasonic bath. During the nucleation phase, a hydrogen feeding flow of 2.5% methane was applied for 15 min at 950 °C (±20 °C). The average growth rate over the entire deposition process was about 15 μm h^{-1}. We estimated the nucleation density to be about 10^{11} cm^{-2}, which is equivalent to a nucleation rate of about 10^7–10^8 cm^{-2} s^{-1}. The nucleation rate reaches its maximum after about 30 min during the process [37–39].

2.2. Tomography by an automated 3D EBSD-FIB technique

A sample ($5 \times 5 \times 4$ mm^3) was cut from the non-freestanding film. The analysis was conducted in a Zeiss XB1560 Crossbeam FIB-SEM consisting of a field-emission electron column and a Ga$^+$ ion emitter. For orientation microscopy, an EBSD detector (TSL/EDAX) was installed at a position opposite the FIB column. This position allows the quick and precise change between FIB milling for serial sectioning (sample at 36°) and EBSD mapping (sample at 70°) [25, 40–43]. The spatial resolution of 3D pixels for EBSD analysis can be as small as $50 \times 50 \times 50$ nm^3.

For serial sectioning the FIB was operated at an accelerating voltage of 30 kV and a milling current of 500 pA. The volume milled between two subsequent sections was 20×20 μm^2 (ND) × 100 nm (milling depth). The milling direction was perpendicular to the cross section of the sample (20 min per slice). After each sectioning step, the sample was tilted into the EBSD position and Kikuchi diffraction patterns were acquired using a 100 nm step size on an area of 20×18 μm^2. Each orientation map

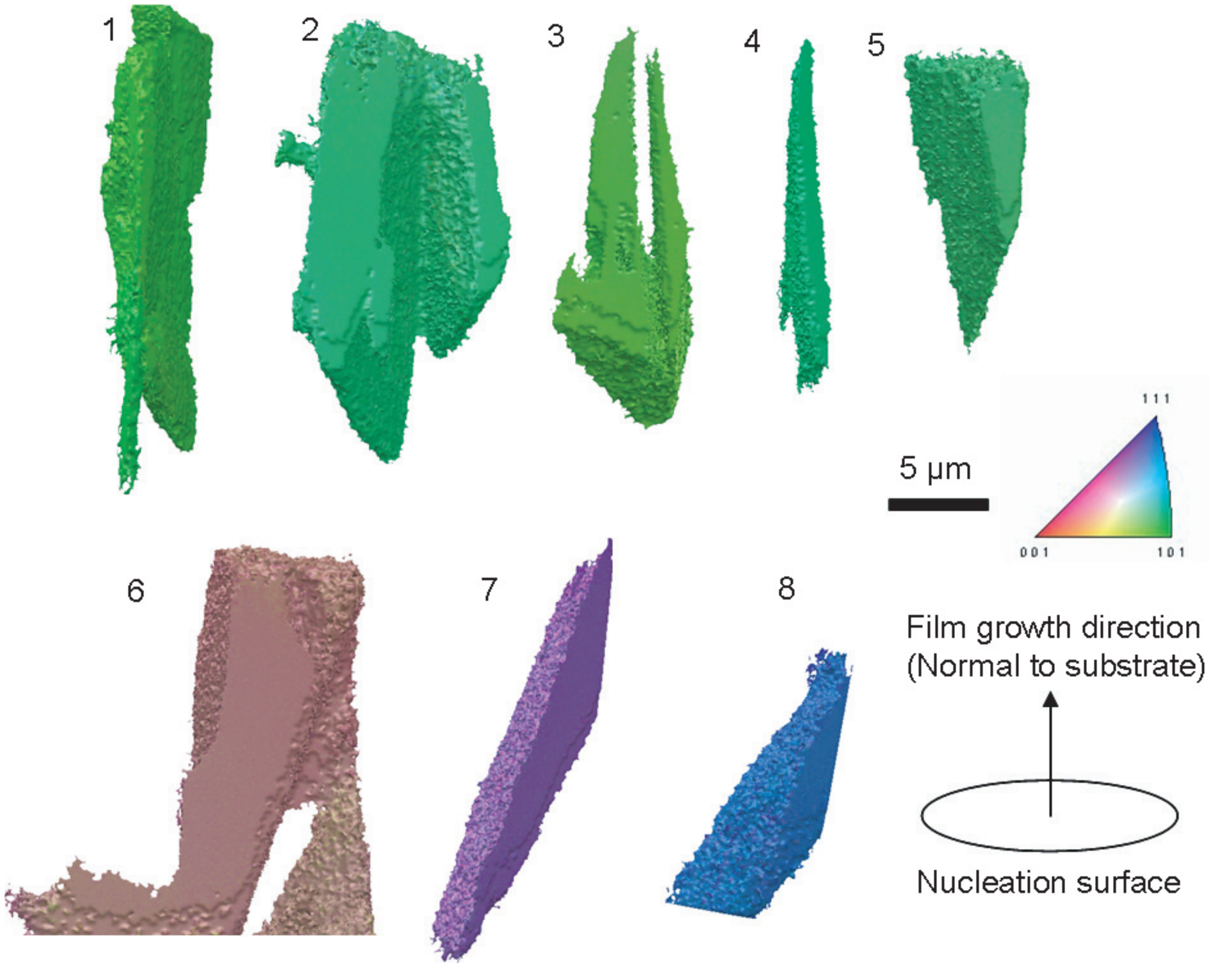

Figure 2. 3D EBSD tomography of eight grains extracted from the 3D image of section 6 in figure 1. The sequence of the eight grains corresponds to the numbering in section 6. Orientation maps are color coded according to the crystallographic direction parallel to the growth direction.

required about 7 min at a frame rate of 150 1 s^{-1}. 2D and 3D microstructure reconstructions were performed using software by TSL/EDAX and our own analysis routines.

3. Results and discussion

3.1. *Effect of FIB and EBSD parameters on data acquisition*

Obtaining a sufficiently high surface quality for EBSD analysis is difficult for diamond. The accelerating voltage and current used during FIB milling have a large effect on the quality of the Kikuchi diffraction patterns since the interaction between the diamond and the Ga^{+} beam produces microstrains in the film. Furthermore, the acquisition of EBSD maps requires a smooth surface finish since roughness may cause shadowing effects. The optimal FIB parameters for minimum roughness are 30 kV accelerating voltage and 500 pA milling current. To obtain accurate EBSD mapping, configuration parameters such as the camera setup, Hough transformation, background processing, and mapping parameters must be carefully tuned.

3.2. *Microstructure and microtexture*

The total volume inspected was $20 \times 20 \times 3.3\ \mu\mathrm{m}^3$ (milled depth, 34 EBSD slices). Figure 1 shows a sequence of sections perpendicular to the growth direction.

Section 1: Some grains are randomly nucleated on the substrate. The ⟨031⟩ growth axis dominates. Further grains appear with ⟨332⟩, ⟨110⟩, and ⟨631⟩ growth directions. Figure 1 reveals that twinning occurs at this initial growth stage. We interpret the nucleation according to a Volmer–Weber type mechanism (3D island growth and strong interaction between the adsorbate [44]) because of the rough nucleation morphology on the substrate.

Section 2: The ⟨031⟩-, ⟨332⟩- and ⟨110⟩-oriented grains continue to grow, as shown in figure 2. A ⟨631⟩-oriented grain that exhibits a twinning relationship with the ⟨031⟩-oriented grain is overgrown, as shown in figure 3. One ⟨001⟩- and two ⟨110⟩-oriented grains are formed and disappear due to overgrowth by neighbor grains. One ⟨110⟩- oriented grain and one ⟨211⟩-oriented grain appear. Furthermore, the ⟨211⟩- and ⟨332⟩-oriented grains grow obliquely to the normal direction of the substrate.

Section 3: The ⟨031⟩-oriented grain grows further. A new ⟨110⟩-oriented grain is nucleated via twinning by another

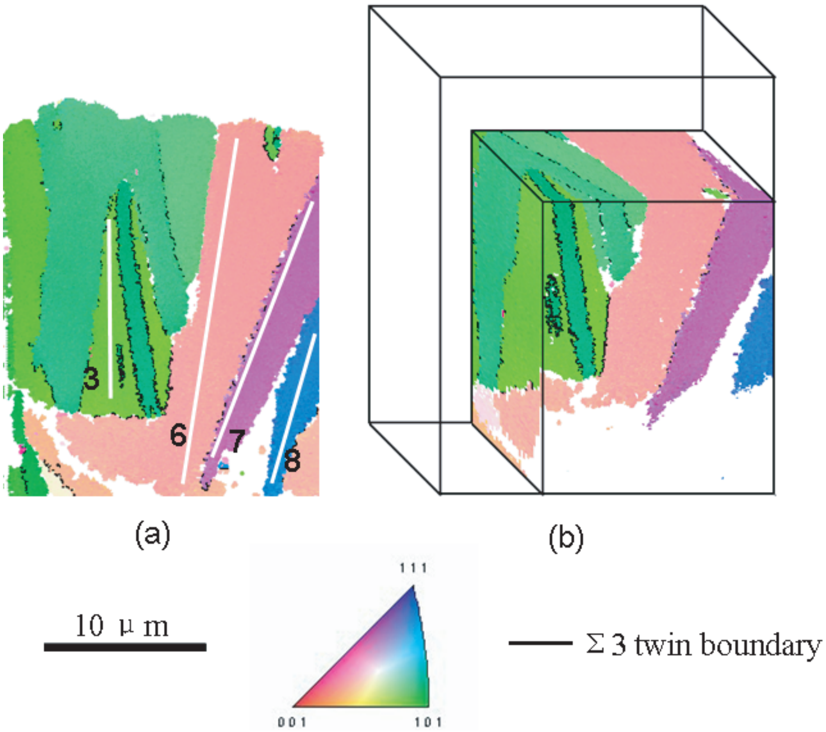

Figure 3. Orientation maps with Σ3 twin boundaries (a) in one of the 2D cross-section slices (11th slice) and (b) in a part of the 3D image. The in-grain misorientation profiles that are shown in figure 4 are computed along the white lines indicated. Orientation maps are color coded according to the growth direction.

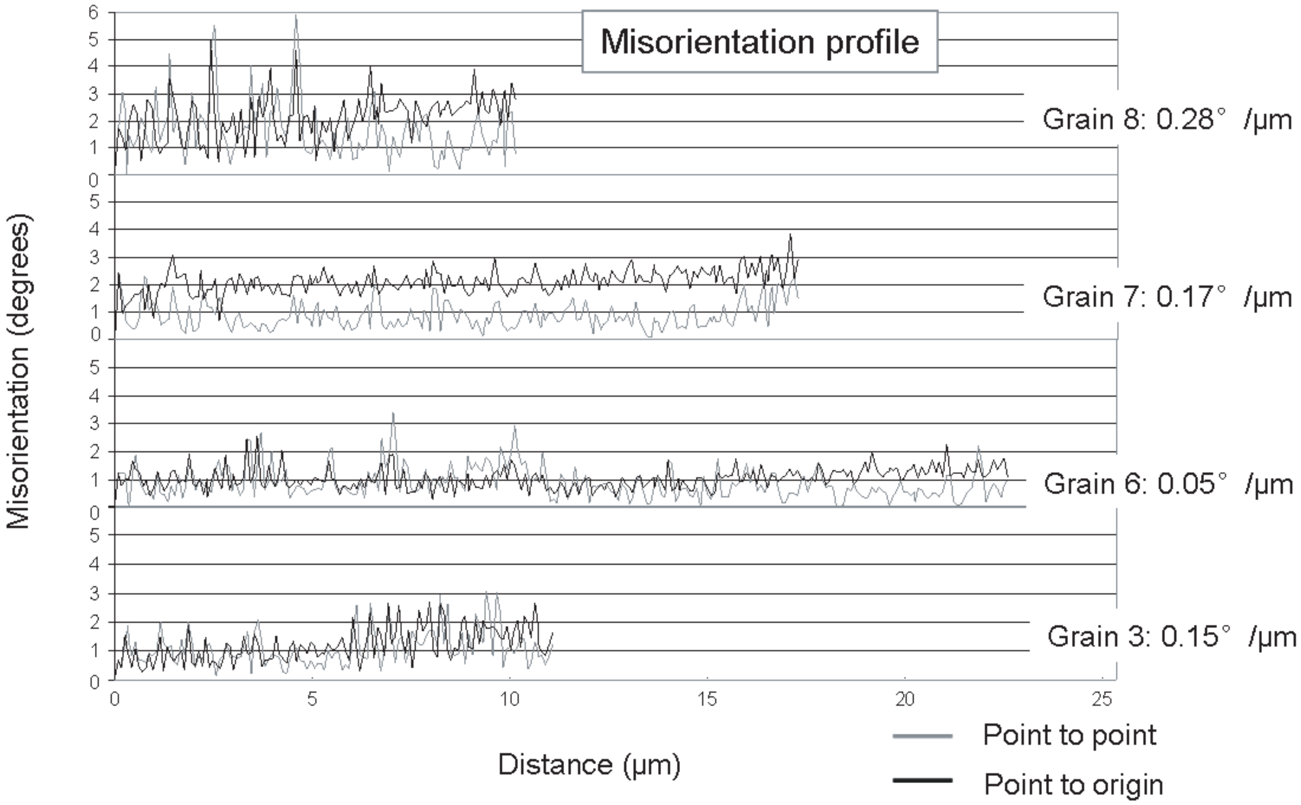

Figure 4. Misorientation profiles in different grains. The point-to-point curves indicate the profiles of the orientation fluctuations between neighboring points. The point-to-origin curves indicate the profiles of the orientation fluctuations between all points and a reference point.

⟨110⟩ grain. Both crystals grow further and have a large volume. The ⟨211⟩- and ⟨332⟩-oriented grains continue to grow obliquely.

Section 4: The ⟨332⟩-oriented grain is overgrown due to its oblique growth and lower growth rate. Similarly, the ⟨211⟩-oriented grain is prevented from further growth by competition. The other grains continue to grow.

Section 5: The ⟨211⟩-oriented grain disappears. A new ⟨110⟩-oriented grain appears via twinning of the ⟨031⟩-oriented grain. All other grains grow vertically.

Section 6: Some ⟨110⟩-oriented grains and one ⟨031⟩-oriented grain eventually prevail due to growth competition after the film thickness reaches approximately 20 μm. Grains 1–5 have a twinning relationship among each other. Also, grains 6 and 7 have a twinning relationship.

In summary, the crystals belonging to the ⟨110⟩ texture fiber tend to grow vertically with respect to the substrate. They have a clear growth advantage over the other grains. The initial ⟨110⟩-oriented crystals that form twins continue to grow together with their twinning orientations. This mechanism leads to large clusters of ⟨110⟩-oriented grains.

Eight individual grains are reconstructed in 3D, as shown in figure 2. The ⟨110⟩-oriented grains (1–5) extend strictly perpendicular to the substrate, suggesting that their growth advantage is due to the absence of twin barriers in the growth direction. All twin facets appear parallel to the growth direction, thus they cannot impede longitudinal growth. The growth shapes can be classified into three types: (1) columnar: the cross section of grain 1 is similar from the bottom to the top; (2) conical: grains 2–4 decrease in cross-sectional area in the longitudinal direction; (3) inverse-conical: grains 5–8 have increasing diameter with increasing film thickness.

3.3. Twinning and in-grain orientation gradients

We observe a number of $\Sigma3$ twin boundaries (58°–62°/⟨111⟩), as shown in figure 3(a). Figure 3(b) shows the twin boundaries in the plane perpendicular to the cross section. Twinning occurs particularly often among ⟨110⟩-oriented grains. The initial and twinned grains grow parallel. The main mechanism for the formation of new grains during growth is twinning. For example, grain 9 is formed by twinning from grain 6, as shown in figure 1.

For some grains, the orientation gradients are analyzed along their longitudinal directions, as indicated by the white lines in figure 3. We obtain gradients of $0.28^\circ\ \mu\mathrm{m}^{-1}$ for grain 8 (⟨332⟩), $0.17^\circ\ \mu\mathrm{m}^{-1}$ for grain 7 (⟨211⟩), $0.15^\circ\ \mu\mathrm{m}^{-1}$ for grain 3 (⟨110⟩), and $0.05^\circ\ \mu\mathrm{m}^{-1}$ for grain 6 (⟨031⟩), as shown in figure 4. The data suggest that oblique grains have higher in-grain orientation gradients. This leads to a higher content of geometrically necessary dislocations in these crystals. This observation suggests that growth along the ⟨110⟩ and ⟨031⟩ directions produces fewer defects and is more stable than growth along the other directions (⟨332⟩ and ⟨211⟩). This might be another reason for the survival of the ⟨110⟩- and ⟨031⟩-oriented grains.

4. Conclusions

An automated 3D tomographic EBSD technique was, for the first time, applied to study the crystallographic 3D growth morphology of a diamond film. The 3D microstructure was investigated from the nucleation stage at the substrate interface until growth termination. ⟨110⟩-oriented grains prevail in the microstructure because of their high growth rate. The more oblique grains are often terminated by the growth of neighbor grains. Also, they exhibit higher in-grain orientation gradients. Twinning occurs frequently during the initial nucleation stage. New grains are formed via twinning rather than by secondary nucleation.

Acknowledgments

The authors are thankful for the financial support of International Max Planck Research School for Surface and Interface Engineering in Advanced Materials (IMPRS-SurMat). We acknowledge the assistance of Igor Schestakow in the experiments.

References

[1] Klein C A 1992 *Mater. Res. Bull.* **27** 1407

[2] May P W 1995 *Endeav. Mag.* **19** 101

[3] Clausing R E 1998 *Handbook of Industrial Diamonds and Diamond Films* (New York: Marcel Dekker)

[4] Clausing R E, Horton L L, Angus J C and Koidl P 1991 *Diamond and Diamond-like Films and Coatings* (New York: Plenum)

[5] Gluche P, Adamschik M, Vescan A, Ebert W, Szücs F, Fecht H J, Flöter A, Zachai R and Kohn E 1998 *Diam. Relat. Mater.* **7** 779

[6] Wild C, Kohl R, Herres N, Müller-Sebert W and Koidl P 1994 *Diam. Relat. Mater.* **3** 373

[7] Spitsyn B V, Bouilov L L and Derjaguin B V 1981 *J. Cryst. Growth* **52** 219

[8] Govindaraju N, Aleksov A, Li X, Okuzumi F, Wolter S D, Collazo R, Prater J T and Sitar Z 2006 *Appl. Phys.* A **85** 331

[9] McCurdy A K 1982 *Phys. Rev.* B **26** 6971

[10] McCurdy A K, Maris H J and Elbaum C 1970 *Phys. Rev.* B **2** 4077

[11] Su Q, Xia Y, Wang L, Liu J and Shi W 2007 *Vacuum* **81** 644

[12] Fabisiak K, Banaszak A, Kaczmarski M and Kozanecki M 2006 *Opt. Mater.* **28** 106

[13] Avigal Y, Glozman O, Etsion I, Halperin G and Hoffman A 1997 *Diam. Relat. Mater.* **6** 381

[14] Goudeau P, Vandenbulcke L, Met C, De Barros M I, Andreazza P, Thiaudiere D and Gailhanouf M 2005 *Surf. Coat. Technol.* **200** 170

[15] Schade A, Rosiwal S M and Singer R F 2006 *Diam. Relat. Mater.* **15** 1682

[16] Himpsel F J, Knapp J A, Van Vechten J A and Eastman D E 1979 *Phys. Rev.* B **20** 624

[17] Dingley D J and Randle V 1992 *J. Mater. Sci.* **27** 4545

[18] Adams B L, Wright S I and Kunze K 1993 *Metall. Trans.* A **24** 819

[19] Schwarzer R A 1997 *Micron* **28** 249

[20] Schwartz A J, Kumar M and Adams B L 2000 *Electron Backscatter Diffraction in Material Science* (New York: Plenum)

[21] Humphreys F J 2001 *J. Mater. Sci.* **36** 3833

[22] Zaefferer S 2005 *Proc. 14th Int. Conf. Textures Mater. ICOTOM 14, Mater. Sci. Forum* **495–497** 3

[23] Fujii S, Shikata S, Uemura T, Nakahata H and Harima H 2005 *IEEE Trans. Ultrason. Ferroelectr. Freq. Control.* **52** 1817

[24] Groeber M, Haley B, Uchic M and Ghosh S 2004 *Materials Processing and Design: Modeling, Simulation and Application Proceedings of NUMIFORM* ed S Ghosh, J Castro and J K Lee (New York: AIP) p 1712

[25] Zaefferer S, Wright I and Raabe D 2008 *Metall. Mater. Trans.* A **39** 374

[26] Lassen N C K, Jensen D J and Conradsen K 1992 *Scanning Microsc.* **6** 115

[27] Wild C, Koidl P and Müller W 1993 *Diam. Relat. Mater.* **2** 158

[28] Tachibana T, Yokota Y, Miyata K, Onishi T and Kobashi K 1997 *Phys. Rev.* B **56** 967

[29] Chen H W and Rudolph V 2003 *Diam. Relat. Mater.* **12** 1633

[30] Smereka P, Li X, Russo G and Srolovitz D J 2005 *Acta Mater.* **53** 1191

[31] Battaile C C, Srolovitz D J and Butler J E 1997 *Diam. Relat. Mater.* **6** 1198

[32] Busch J V and Dismukes J P 1994 *Diam. Relat. Mater.* **3** 295

[33] Kobashi K 2005 *Diamond Films* (Amsterdam: Elsevier)

[34] Lu F X, Tang W Z, Huang T B, Lin J M, Song J H, Yu W X and Tong Y M 2001 *Diam. Relat. Mater.* **10** 1551

[35] Iijima S, Aikawa Y and Baba K 1990 *Appl. Phys. Lett.* **57** 2646

[36] Anger E, Giequel A, Wang Z Z and Ravet M F 1995 *Diam. Relat. Mater.* **4** 759

[37] Liao K J, Wang W L and Feng B 1998 *Phys. Status Solidi* a **167** 117

[38] Ye H, Sun C Q, Hing P, Xie H, Zhang S and Wei J 2000 *Surf. Coat. Technol.* **123** 129

[39] Gnedenkov S V, Khrisanfova O A, Zavidnaya A G, Sinebrukhov S L, Kovryanov A N, Scorobogatova T M and Gordienko P S 2000 *Surf. Coat. Technol.* **123** 24

[40] Konrad J, Zaefferer S and Raabe D 2006 *Acta Mater.* **54** 1369

[41] Zaafarani N, Raabe D, Singh R N, Roters F and Zaefferer S 2006 *Acta Mater.* **54** 1707

[42] Bastos A, Zaefferer S and Raabe D 2008 *J. Microsc.* **230** 487

[43] Zaafarani N, Raabe D, Roters F and Zaefferer S 2008 *Acta Mater.* **56** 31

[44] Volmer M and Weber A 1926 *Z. Phys. Chem.* **119** 277